

1           **Assimilation of Himawari-8 Imager Radiance Data with the WRF-3DVAR**  
2                                   **system for the prediction of Typhoon Soudelor**

3           **Feifei Shen<sup>1,2,3\*</sup>, Aiqing Shu<sup>1</sup>, Hong Li<sup>4</sup>, Dongmei Xu<sup>1,2,3</sup>, Jinzhong Min<sup>1</sup>**

4  
5           1. *The Key Laboratory of Meteorological Disaster, Ministry of Education*  
6           *(KLME)/Joint International Research Laboratory of Climate and Environment*  
7           *Change (ILCEC)/Collaborative Innovation Center on Forecast and Evaluation of*  
8           *Meteorological Disasters (CIC-FEMD), Nanjing University of Information Science &*  
9           *Technology, Nanjing 210044, China*

10          2. *Heavy Rain and Drought-Flood Disasters in Plateau and Basin Key Laboratory*  
11          *of Sichuan Province, Chengdu, China*

12          3. *The Institute of Atmospheric Environment, China Meteorological Administration,*  
13          *Shenyang 110000, China*

14          4. *Shanghai Typhoon Institute, China Meteorological Administration, Shanghai*  
15          *200030, China*

19 **Abstract**

20 Himawari-8 is a new generation geostationary meteorological satellite launched  
21 by Japan Meteorological Agency. It carries the Advanced Himawari Imager (AHI)  
22 onboard, which can continuously monitor high-impact weather events with high  
23 frequency space and time. The assimilation of AHI radiance data was implemented  
24 with the three-dimensional variational data assimilation system of Weather Research  
25 and Forecasting model for the analysis and prediction of Typhoon Soudelor (2015) in  
26 the Pacific Typhoon season. The effective assimilation of AHI radiance data in  
27 improving the forecast of the tropical cyclone during its rapid intensification has been  
28 realized. The results show that after assimilating the AHI radiance data under clear  
29 sky conditions, the typhoon position in the background field of the model was  
30 effectively corrected compared with the control experiment without AHI radiance data  
31 assimilation. It is found that the assimilation of AHI radiance data is able to improve  
32 the analyses of the water vapor and wind in typhoon inner-core region. The analyses  
33 and forecasts of the minimum sea level pressure, the maximum surface wind, and the  
34 track of the typhoon are further improved.

35 **Key words:** Weather Research and Forecasting model; Three-Dimensional  
36 Variational Data Assimilation; AHI Radiance Data; Typhoon

37

## 38 **1. Introduction**

39 In recent years, although researchers have made great progress in the field of  
40 numerical weather prediction (NWP), the huge challenges are encountered in the  
41 accurate forecasts of tropical cyclones (TCs) with rapid intensifications (DeMaria et  
42 al., 2014). The predictability of these TCs is limited because it entails complex  
43 multi-scale dynamic interactions (Minamide and Zhang 2018). These interactions  
44 include environmental airflows, TC vortex interactions, atmosphere-ocean  
45 interactions, and the effects of mesoscale and micro-convective scale, together with  
46 the microphysics and atmospheric radiation. In order to attain a better initial condition  
47 and improve the accuracy of the forecast, data assimilation seeks to fully utilize the  
48 observations. The life span of most TCs is over the ocean where conventional  
49 observations are relatively insufficient compared to the land. Therefore, by analyzing  
50 observed data from satellites and planes over the ocean, it is crucial to adopt effective  
51 data assimilation (DA) methods to improve the analysis and forecast of TCs.

52 With the rapid development of atmospheric radiative transfer model, many  
53 numerical weather prediction centers have adopted variational DA method to  
54 assimilate a variety of radiance data from different satellite observation instruments  
55 (Bauer et al., 2011; Buehner et al., 2016; Derber et al., 1998; Hilton et al., 2009;  
56 Kazumori et al., 2014; McNally et al., 2006; Prunet et al., 2000). These data can take  
57 up 90% of all data used in global DA system and can improve the accuracy of the  
58 numerical model results strikingly (Bauer et al., 2010). Some researches demonstrated

59 that in global model, satellite radiance DA makes more contribution to improving the  
60 accuracy of the numerical model results than conventional observation DA does  
61 (Zapotocny et al., 2007, Yan et al., 2010; Geer et al., 2017).

62 Generally speaking, radiance data are derived from microwave and infrared  
63 detecting instruments, which are from polar-orbit satellites and geostationary satellites,  
64 respectively. Polar-orbit satellites cover the sphere of all the earth, thereby suitable for  
65 global NWP models (Jung et al., 2008). Besides, they have finer resolutions compared  
66 to geostationary satellites (Li et al., 2017; Shen et al., 2015; Xu et al., 2013). However,  
67 it is highlighted that they are not able to generate continuous observations for a fixed  
68 regional area and so may miss rapidly intensified TCs or storms. On the contrary,  
69 because geostationary satellites rotate with the earth, although their resolutions are  
70 lower than that of polar-orbit satellites, they can capture the formation and  
71 development of mesoscale convective systems by continuous monitoring (Montmerle  
72 et al., 2007; Stengel et al., 2009; Zou et al., 2011).

73 Geostationary satellites are able to continuously detect a region at a higher  
74 frequency, thus observing TCs over the vast ocean effectively. As the first new  
75 generational geostationary satellite, Himawari-8 plays a pioneering role for the  
76 geosynchronous imagers to be launched in US, China, Korea and Europe. It has an  
77 advanced imager called Advanced Himawari Imager (AHI) with 16 visible and  
78 infrared bands, including 3 moisture channels, which can conduct a full-disk scan  
79 every 10 minutes. Meanwhile, it can also acquire regional scanning images and that is

80 to say it can scan the Japan and the target areas every 2.5 minutes. Compared to the  
81 early geosynchronous imagers, AHI has more spectrum bands and this can monitor  
82 the state of atmosphere with a higher frequency.

83 In recent years, some experts and scholars have carried out some studies on the  
84 data assimilation of geostationary satellite observations. Firstly utilizing Gridpoint  
85 Statistical Interpolation (GSI) from National Centers for Environmental Prediction  
86 (NCEP), Zou, et al (2011) conducted direct assimilation on imagers' data from  
87 GOES-11 and GOES-12 to estimate their potential influences on quantitative  
88 precipitation forecasts (QPF) of coastal regions in the eastern part of American. They  
89 found that assimilating radiance data from GOES's imager has a remarkable  
90 improvement on 6 to 12 hour's QPF near northern Mexico Gulf coast. Their work was  
91 continued by Qin, et al (2013), which put thinned radiance data into GSI system to  
92 make a comprehensive investigation on the issue on combined assimilation of GOES  
93 Imager data together with Advance Microwave Sounding Unit-A (AMSU-A),  
94 Advance Microwave Sounding Unit-B (AMSU-B), Atmospheric Infrared Sounder  
95 (AIRS), Microwave Humidity Sounder (MHS), High Resolution Infrared Radiation  
96 Sounder (HIRS), GOES Sounder (GSN). The results showed the effect of single  
97 assimilation of AHI radiance data are better than combined assimilation in term of  
98 precipitation forecast. Zou, et al (2015) adopted the GSI system to assimilate radiance  
99 data from four infrared channels on GOES-13/15 and set up two experiments for  
100 comparison. A symmetric vortex was used for initialization in the first experiment and

101 an asymmetric counterpart for the other experiment. Results showed that direct  
102 assimilation of GOES-13/15's radiance data could yield positive effects on the track  
103 and intensity forecasts of hurricane "Debbie". As the new instrument of himawari-8,  
104 there are few studies on the DA of himawari-8 data. Ma, et al (2017) used  
105 four-dimensional ensemble variational (4DEnVar) DA in NCEP's GSI system to  
106 assimilate radiance of three moisture channels of AHI radiance data under clear-sky  
107 condition and then NCEP Global Forecast System (GFS) was utilized to estimate the  
108 impacts of AHI radiance data assimilation on weather forecast. They found it had a  
109 positive impact on the forecast of global vapor at high level of troposphere. Wang, et  
110 al (2018) investigated the impact of assimilating three water vapor channels under  
111 clear sky on the analysis and forecast of a rainstorm in Northern China with the  
112 3DVAR method. It pointed out that the assimilation of AHI radiance data could  
113 improve the wind and vapor fields and the accuracy of rainfall forecast in the first 6  
114 hours lead time.

115 Although previous researches have made several achievements in satellite data  
116 assimilation and application, it is still a challenge to make more effective use of the  
117 new generational geostationary satellite imager data with high spatial and temporal  
118 resolution. In most of the previous studies, researches usually use a 6 hour's or even  
119 longer time interval with a coarse spatial resolution. Therefore, the rapid updating  
120 assimilation techniques of the geostationary satellite radiance data have not been well  
121 carried out at convective scale. This study intends to build a data assimilation system

122 aiming at AHI radiance data based on the new generational mesoscale Weather  
123 Research and Forecasting (WRF) model. A case of Typhoon Soudelor is studied by  
124 performing numerical simulation to address the impacts of convective DA on the  
125 improvement of the initial conditions of TC and the enhancement of track and  
126 intensity forecasts. Our study focuses mainly on assimilating the three water vapor  
127 channels (6.2, 6.9, and 7.3 $\mu$ m) since they are very sensitive to the humidity in the  
128 middle and upper troposphere and have a certain effect on the lower troposphere.  
129 Thus, a large amount of effective atmospheric information can be provided for AHI  
130 radiance data assimilation in the troposphere. The weighting functions for the three  
131 channels are provided in Fig. 1.

132 Section 2 describes the observations and the data assimilation system. Introductions  
133 to the typhoon case and the experimental setup are provided in section 3. The detailed  
134 results in terms of the analyses and the forecasts are illustrated in section 4 before  
135 conclusions are summarized in section 5.

## 136 **2. Observational data and DA system**

### 137 *2.1 An introduction to Himawari-8 AHI radiance data*

138 Himawari-8 satellite was launched by JMA to a geosynchronous orbit on 17  
139 October 2014 and has begun its operational use since 7 July 2015 (Bessho et al.,  
140 2016). It is located between the equator and 140.7°E, thus the earth is observed  
141 between 60°N and 60°S meridionally and between 80°E and 160°W zonally.  
142 Compared to its previous generation Himawari-7, its detective ability can get

143 significantly improved since the instrument AHI on Himawari-8. Besides, its device is  
144 comparable to imagers on American GOES-R satellite (Goodman et al., 2012; Schmit  
145 et al., 2005; Schmit et al., 2008; Schmit et al., 2017). AHI is able to provide a full-disk  
146 image every 10 minutes and complete a scan over Japan every 2.5 minutes. AHI  
147 conducts continuous scan and detection on a moving targeted typhoon. It has 16  
148 channels covering visible, near-infrared, and infrared spectral bands with a resolution  
149 of 0.5 km or 1 km, and 2 km respectively. Channel 8 to 10 (6.2, 6.9, and 7.3  $\mu\text{m}$ ) are  
150 water vapor bands that are sensitive to the humidity in the middle and upper  
151 troposphere (Di et al., 2016). Other channels (channel 11, 12, 16: 8.6  $\mu\text{m}$ , 9.6  $\mu\text{m}$ , and  
152 13.3 $\mu\text{m}$  ) are either monitoring other fields such as the thin ice clouds, volcanic  $\text{SO}_2$   
153 gas, the ozone or  $\text{CO}_2$ , or the atmospheric window channels (13-15: 10.4, 11.2, and  
154 12.4  $\mu\text{m}$ ) function as monitors for ice crystal/water, low water vapor, volcanic ash, sea  
155 surface temperature and other phenomena (Bessho et al., 2016).

## 156 *2.2 WRFDA system and AHI radiance data*

157 WRFDA system is designed by National Center for Atmospheric Research  
158 (NCAR) and it contains 3DVAR, 4DVAR, Hybrid parts. This research is based on the  
159 3DVAR method. An interface that is suitable for AHI DA is built in WRFDA system.  
160 Currently, WRFDA is able to assimilate many conventional and unconventional  
161 observations. In terms of satellite radiance data, this system is compatible with the  
162 Radiative Transfer model of the Television and Infrared Observational Satellite  
163 Operational Vertical sounder (RTTOV) and Community Radiative Transfer Model



164 (CRTM, Liu and Weng, 2006) as observation operators. In this study, CRTM is  
165 utilized as the observation operator to simulate and compute AHI radiance data.  
166 Estimating the systematic bias and random error of the observations caused by the  
167 errors of numerical models and instruments are the key factors to directly assimilate  
168 the satellite radiance data. Apart from eliminating cloud pixels, other procedures are  
169 implemented inside the data assimilation framework for the quality control are as  
170 follows. (1) when reading the data, remove the observed outliers with values below 50  
171 K or above 550 K; (2) only the marine observations are applied by removing the  
172 observations on the land and the observations over complex surfaces; (3) remove  
173 observations when the observation minus the background is larger than 3 times of the  
174 observation error; (4) the pixels are removed when the cloud liquid water path  
175 calculated by the background field of the numerical model is greater than or equal to  
176 0.2 kg/m<sup>2</sup>; (5) eliminate the data when the observation minus background is greater  
177 than 5 K. These two parameters are used for these radiances on different sensors of  
178 various satellites such as AMSU-A, MHS, and the Advanced Microwave Scanning  
179 Radiometer 2 (AMS2) (Wang et al., 2018, Yang et al., 2016).

180 By using 3DVAR algorithm, the assumption is that there is no bias between  
181 observation and background (Dee et al., 2009; Liu et al., 2012; Zhu et al., 2014). A  
182 bias correction scheme for observation is essential before DA. Usually, radiance bias  
183 can be obtained by a linear combination of a set of forward operators.

184 
$$\tilde{H}(x, \beta) = H(x) + \beta_0 + \sum_{i=1}^{N_p} \beta_i p_i \quad (1)$$

185 Here,  $H(x)$  represents the initial observation operator (before the bias  
 186 correction) and  $x$  represents the mode state vector.  $N_p$  is the number of the  
 187 predictions.  $\beta_0$  represents a constant component of the total bias (constant part),  
 188 while  $p_i$  and  $\beta_i$  represent the  $i$ -th predictor and its coefficient respectively. In this  
 189 study, four potentially state-dependent predictors (1000–300 hPa and 200–50 hPa  
 190 layer thicknesses, surface skin temperature, and total column water vapor) are applied.  
 191 The variational bias correction (VarBC) scheme is utilized to update the bias  
 192 correction coefficient variationally with the new observation operator considered in  
 193 the cost function of 3DVAR.

194 **3. Introduction to the typhoon and experimental design**

195 *3.1 Typhoon Soudelor*

196 From the record of the China Meteorological Administration (CMA), Typhoon  
 197 Soudelor was the 13th typhoon in 2015 as the second strongest tropical cyclone in that  
 198 year. At 1200 UTC 30 July 2015, it formed at northwest Pacific Ocean as a tropical  
 199 storm at 13.6° N, 159.2° E, then moved north-westwards. It upgraded to a strong  
 200 tropical storm at 2100 UTC 1 August 2015. Afterwards, it went through a process of  
 201 rapid intensification. It became a typhoon at 0900 UTC 2 August 2015, a strong  
 202 typhoon at 2100 UTC 2 August 2015, a super typhoon at 0900 UTC 3 August 2015.  
 203 Then it weakened to a strong typhoon in the morning on 5 August 2015. However, it

204 intensified to a super typhoon again at 1200 UTC 7 August 2015 with a maximum  
205 surface wind of  $52 \text{ m s}^{-1}$ , moving west by north, and its intensity raised to its second  
206 peak. It was reduced to a strong typhoon again at 1800 UTC 7 August 2015. It  
207 decreased to a typhoon, entering to Taiwan Strait. It landed again as a typhoon at 1410  
208 UTC on the coast of Fujian Province, China. Owing to continuous orographic friction,  
209 it decreased to a tropical depression. Fig. 2 shows the track of Soudelor and different  
210 color lines represent typhoon's maximum surface wind. It is displayed that after the  
211 formation of typhoon, its track is relatively stable. After July 30, the tropical  
212 depression moved west by north at a speed of about 20 km/h. Its moving tendency  
213 changed slightly within 10 days of its generation. However, its intensity went through  
214 a rapid intensification, a weakening, a second intensification, following by a  
215 continuous weakening after landing on the China. Fig. 3 demonstrates the variation of  
216 typhoon's intensity from 31 July 2015 to 5 August 2015. It is shown that typhoon's  
217 maximum surface wind increased fast, while its minimum sea level pressure  
218 decreased sharply. This was the stage of typhoon's rapid intensification. The period  
219 from 1 August 2015 to 3 August 2015 during its rapid intensification is selected.

### 220 *3.2 Experimental design*

221 Two experiments are designed to investigate the effects of AHI radiance data  
222 direct assimilation on the analysis and forecast of Typhoon Soudelor starting from  
223 1800 UTC 1 August 2015 to 0000 UTC 3 August 2015. WRF 3.9.1 is employed as the  
224 forecast model in this experiment. Arakawa C grid is used in the horizon with a 5 km

225 grid distance. As is known, Arakawa A grid is "unstaggered" by evaluating all  
226 quantities at the same point on each grid cell. The "staggered" Arakawa B-grid  
227 separates the evaluation of the velocities at the grid center and masses at grid corners.  
228 Arakawa C grid further separates evaluation of vector quantities compared to the  
229 Arakawa B-grid. Vertically, it has 41 eta levels using 10 hPa as its top with coarser  
230 vertical spacing for the higher levels. The center of the model domain is located at  
231 (17.5 °N, 140 °E) (Fig. 4). The initial condition and lateral boundary are provided by  
232 0.5°×0.5° Global Forecasting System (GFS) reanalysis data. The following  
233 parameterization schemes are used: The following parameterization schemes are used:  
234 WDM6 microphysics scheme (Lim et al., 2010), Grell Devenyi cumulus  
235 parameterization scheme (Grell et al., 2002), Rapid Radiative Transfer Model (RRTM)  
236 longwave radiation scheme (Mlawer et al., 1997), shortwave radiation scheme  
237 (Dudhia et al., 1989), and YSU boundary layer scheme (Hong et al., 2006) .

238 The experimental procedures are illustrated by Fig. 5. Firstly, a 6-hour's spin-up  
239 conducted initialized from 1800 UTC 1 August 2015 to prepare the background field  
240 for the data assimilation at 0000 UTC 2 August 2015. The 6-hour spin-up period is  
241 commonly applied to initialize the typhoon or hurricane system the data assimilation  
242 experiments, although longer spin-up period is also acceptable to introduce more  
243 model errors in the background such as 12-hour or 24-hour. The first experiment is  
244 assimilating GTS (Global Telecommunications System) conventional data (including  
245 aircraft report, ship report, sounding report, satellite cloud wind data, ground station

246 data) only, which is called control experiment (CTNL). Another experiment is  
247 configured with AHI radiance data assimilation (AHI\_DA). AHI radiance data is  
248 assimilated hourly further from 0000 UTC to 0600 UTC on 2 August 2015.  
249 Afterwards, a 48 hours forecast is launched as the deterministic forecast. The  
250 climatological background error (BE) statistics are estimated using the National  
251 Meteorological Center (NMC) method. There are 5 control variables applied in this  
252 study including U component, V component, full temperature, full surface pressure,  
253 and pseudo-relative humidity. The observation error for each channel is estimated  
254 based on the observed brightness temperature minus background brightness  
255 temperature (OMB) from 0000 UTC on 1 August 2015 to 0000 UTC on 3 August  
256 2015 every 6 hours.

257 Fig. 4 also shows the distribution of GTS observation data at the simulated  
258 domain at 0000 UTC 2 August 2015. It is proved that raw radiance observations  
259 thinned to a grid with 2–6 times of the model grid resolution are able to remove the  
260 potential error correlations between adjacent observations (Schwartz et  
261 al., 2012; Xu et al., 2015; Choi et al., 2017). Hence, 20 km is chosen to make  
262 thinning of AHI radiance data. Also, sensitivity experiments with 25 km, and 30 km  
263 thinning mesh are also conducted with similar results (Wang et al., 2018). The length  
264 scale and the variance scale are set to be 0.5 and 1 respectively after several  
265 sensitivity experiments conducted on tuning the background error. Similar  
266 conclusions are also found in Shen and Min (2015) with the scale factors related to

267 the static background error covariance.

## 268 **4. Results**

### 269 *4.1 Minimization iterations*

270 In this study, minimization stops when the norm of the gradient for the cost  
271 function is reduced by a factor of 0.01, which is commonly used in data assimilation  
272 procedures. Inner minimization stops either when the criterion of the cost function  
273 gradient is met or when inner iterations reach 200. Fig. 6 shows the cost function and  
274 gradient with the iteration times. It is found that, for this case, the criterion of the cost  
275 function gradient decrease is met. There is an obvious exponential decrease curve in  
276 Fig. 6a, while Fig. 6b shows gradient decreases with the increase of iteration times. It  
277 is seen from Fig. 6a that cost function decreases remarkably in the first 10 iterations.  
278 However, after 30 times of iteration, the cost function curve becomes smooth  
279 gradually. The differences between background field and observation were largest.  
280 With continuous iterations, background field goes through continued adjustments.  
281 Finally, the cost function tended to reach a stable minimum that represents the point  
282 when cost function has its optimal solution. Besides, the gradient in Fig. 6b decreases  
283 generally with increasing iterations. The exponential decrease of the cost function and  
284 the change trend of its gradient indicate that the effectiveness of AHI radiance DA.  
285 The final iterated analytical field was close to the observation. The wall clock times  
286 used by CTNL and AHI\_DA for the data assimilation procedures are rather  
287 comparable with roughly 30 minutes and 40 minutes on a Linux workstation with 36

288 processors. It should be pointed out that computational cost of the deterministic  
289 forecast and the pre-process for gridded GFS data are same in these two experiments.

#### 290 *4.2 Analytical results of the brightness temperature*

291 Figs. 7a, c, and, e show the distribution of OMB, while the observed brightness  
292 temperature minus the simulated brightness temperature from the analyses (OMA)  
293 after the bias correction of AHI radiance data are presented in Figs. 7b, d, and f from  
294 channels 8, 9, and 10 at 0000 UTC 2 August 2015. It should be pointed that even only  
295 parts of the AHI radiance data (roughly 20000 clear sky pixels of total 50000 pixels  
296 for each DA cycle) are applied after quality control in the data assimilation, the  
297 radiative transfer model is able to simulate the brightness temperature for all the  
298 model grid point with the background and the analysis respectively for the verification  
299 purpose. The similar verification method is also applied in Yang et al., (2016). In the  
300 Fig. 7a, part of typhoon's spiral cloud belt was clearly visible. The brightness  
301 temperature in typhoon's inner-core area was low, while the brightness temperature in  
302 other areas was high. The mean of observed OMB was -4.65 K, indicating that the  
303 background brightness temperature was higher than the observation. It is found in Fig.  
304 7b that the OMA values of most pixels were below 0.02 K, indicating that the  
305 analytical field fitting the observation after analyzing. It can be inferred from Figs. 7a,  
306 c, and e that the magnitude in OMB of channel 10 was generally larger than that of  
307 channel 9, while that of the OMB in channel 8 was the smallest. This is because the  
308 detection height of channel 10 was lower than that of channel 8 and 9 seen from the

309 weighting function (Fig. 1), indicating channel 10 is largely affected by the clouds.  
310 Conversely, the weighting peak of the channel 8 was the highest, being least affected  
311 by the clouds. In general, the simulated brightness temperature from the analyses  
312 matched well with the observed brightness temperature of all the three water vapor  
313 channels after the assimilation of AHI radiance data.

314 To validate the effect of the bias correction for AHI radiance data at 0000 UTC 2  
315 August 2015, the scatter plots of the observed brightness temperature and the  
316 brightness temperature from the background before the bias correction are shown in  
317 Figs. 8a, d, and g. Similarly, the results after the bias correction are provided in Figs.  
318 8b, e, and h. From Fig. 8a, before the bias correction, the values from the observation  
319 and the background were comparable, but most of the scatter points were below the  
320 diagonal line. This suggests that the observed brightness temperature was higher than  
321 the background simulated brightness temperature. From Fig. 8b, after the bias  
322 correction, the observed warm bias was corrected to some extent with the root mean  
323 square error (RMSE) of OMB decreasing from 1.864 K to 1.627 K and the average  
324 decreasing from 0.956 K to 0.358 K. The scatter plots of the observed brightness  
325 temperature and the brightness temperature from the analyses after the bias correction  
326 are shown in Figs. 8 c, f, and j. Compared to the result of Fig. 8b, the scatters in Fig.  
327 8c were more symmetrical, fitting closely to the diagonal line. The mean and RMSE  
328 were also significantly reduced, suggesting that the analytical fields match better with  
329 the observation than background field. Among them the RMSEs of channel 10 are  
330 smallest compared to those from channels 8 and 9 for the OMB and OMA samples,  
331 which is likely related to strict cloud detection scheme for channel 10 with rather  
332 lower detecting peak (Wang et al., 2018).

333 Fig. 9 shows the observation numbers, the mean, and the standard deviation of  
334 OMB and OMA of channels 8, 9, and 10 before and after the bias correction. It can be



335 seen that after the quality control, 24057, 24181, 21785 observations are adopted in  
336 the DA system for channels 8, 9, and 10, respectively. From the mean value of OMB  
337 before the bias correction, the value of the three channels was relatively small,  
338 indicating that the simulated brightness temperature of the three channels was close to  
339 the observed brightness temperature. The lowest mean of 0.3 K was found in channel  
340 10, indicating that the simulated brightness temperature of channel 10 was closest to  
341 the observed brightness temperature. Bias correction effectively corrected the  
342 systematic bias and reduces the mean value of observation residuals. After the bias  
343 correction, the OMB mean value of the three channels significantly decreases to  
344 nearly 0 K. With the bias correction, the simulated brightness temperature was almost  
345 the same as the observed brightness temperature. The standard deviations (stdv) of  
346 OMB were comparable before and after the bias correction, since they are calculated  
347 by subtracting the mean of the bias. It is found that the bias was corrected effectively  
348 with an overall same magnitude of bias for each pixel, leading the stdv almost same  
349 before and after the bias correction. The standard deviation of OMA decreased by  
350 about 80% compared to OMB, indicating that the analyses fit better with the  
351 observations after the data assimilation. Differences between the standard deviations  
352 of the OMB and OMA were statistically significant at the 95% level using zero  
353 difference for the null hypothesis.

354 The RMSEs of the simulated brightness temperature by the NWP model before  
355 and after the assimilation are also calculated against the AHI radiance observations.

356 Fig. 10 shows the RMSEs during the DA cycles for channels 8, 9, and 10. As can be  
357 seen from Fig. 10, RMSE decreased after each analysis in AHI\_DA. The most  
358 significant improvement was from the first analysis cycle of channel 8, where RMSE  
359 of the brightness temperature after assimilation significantly decreases from 1.64 K to  
360 0.46 K, possibly due to the largest adjustment on the background for the first analysis  
361 time. The background before the assimilation was the short-term forecast from the  
362 previous analysis. The increase of the RMSE in the fluctuation arised from the model  
363 error in the 1 hour short-term forecast. Overall, the effect of the analysis from the  
364 channel 10 was most significant.

#### 365 *4.3 Analysis of the typhoon structure*

366 Fig. 11 shows the wind field at sea level and the distribution of water vapor at  
367 850 hPa at 0000 UTC 2 August 2015. The obvious cyclonic eddy circulation  
368 structures in the core area of the typhoon are found in both fields, while the  
369 anti-cyclonic circulation existed in the northwest quadrant of the typhoon. The mixing  
370 ratio of water vapor in the region where the typhoon located was very high and the  
371 wind field is cyclonic, indicating that the typhoon has a continuous water vapor  
372 advection. This contributed to the enhancement of typhoon (Kamineni, et al., 2003).  
373 From the flow field of the control experiment in Fig. 11a, the water vapor  
374 convergence in the center of the typhoon region was weak with the low intensity and  
375 smaller coverage. As can be seen from Fig. 11b, after the assimilation of AHI radiance  
376 data, the streamlines in the typhoon region become denser, indicating that the cyclonic

377 circulation was strengthened. Conversely, the intensity and distribution of the water  
378 vapor after the assimilation of AHI radiance data tend to contribute to the developing  
379 typhoon. This suggests that the field outside of the typhoon center was also adjusted  
380 as the assimilation of AHI radiance data was able to improve the large-scale  
381 environmental field in the simulation region of Typhoon Soudelor. It should be  
382 pointed out that the model status in the cloudy area was modified due to the spatial  
383 correlation in the background error covariance. The similar findings for small-scale  
384 information in the cloudy area can also be referred in Wang et al., (2018).

#### 385 *4.4 Track forecast*

386 In order to further evaluate the effect of AHI radiance data assimilation, a 48-hour  
387 deterministic forecast was launched with the analyses initialized from 0000 UTC 2  
388 August 2015 and 0600 UTC 2 August 2015 respectively. The best track data are  
389 provided by the CMA (Yu et al., 2007; Song et al., 2010). The improvement is most  
390 obvious at the start and end point. As can be seen in Fig. 12a, at the beginning of the  
391 forecast, the initial location of the typhoon from the CTNL experiment has large south  
392 bias and east bias at 0000 UTC and 0600 UTC respectively. Conversely, the location  
393 of the typhoon in AHI\_DA is relatively closer to the observation at the beginning..  
394 During the following few hours of forecasts, the typhoon track predicted by the CTNL  
395 continues to show a south-west bias with the environmental wind, while the track  
396 predicted by AHI\_DA match better with the best track. Fig. 12c shows the averaged  
397 typhoon track error over the two forecasts predicted by the two experiments. At the

398 initial time of the forecast, the track errors of CTNL and AHI\_DA were significantly  
399 different, with the magnitude of 55.6 km and 13.4 km, respectively. During the  
400 subsequent 48-hour forecast, the track error of the CTNL gradually increases with the  
401 forecast time reaching 167.1 km at the end of the forecast. In contrast, the track error  
402 of AHI\_DA is consistently less than 122.5 km during the 48-hour forecast period. In  
403 general, the average track error of the CTNL is 168.57 km, and the average track error  
404 of AHI\_DA experiment is only 67.0 km, indicating a significant improvement in the  
405 track prediction.

406 Fig. 13 provides the time series of the typhoon intensity from the two  
407 experiments in terms of the averaged maximum surface wind and minimum sea level  
408 pressure error over the two forecasts initialized from 0000 UTC 2 August 2015 and  
409 0600 UTC 2 August 2015 respectively. It can be seen that the maximum surface wind  
410 error predicted by the AHI\_DA was much lower than that by the CTNL for the first 30  
411 hours, due to the overall under estimation for the intensity of Typhoon Soudelor  
412 simulated in the background field. The maximum surface wind errors of AHI\_DA are  
413 generally smaller than those of CTNL. It should be pointed out that the difference  
414 between the maximum surface wind errors of the two experiments reaches up to 7.5 m  
415 s<sup>-1</sup> after 24-hour forecast. In Fig. 13b, the results of the minimum sea level pressure  
416 are consistent with Fig. 13a, while the improvement for the minimum sea level  
417 pressure lasts for 40 hours.

418 **5. Conclusion**

419 An interface for AHI radiance data assimilation on the WRFDA system based on  
420 the 3DVAR assimilation method was built. Based on the Typhoon Soudelor in 2015,  
421 two experiments for comparison was designed to examine the impact of AHI water  
422 vapor channel radiance data assimilation on the analysis and prediction of the rapid  
423 development stage of Typhoon Soudelor under clear sky condition. Following  
424 conclusions are obtained:

425 (1) The AHI radiance data on the new generation of geostationary meteorological  
426 satellite is able to reflect the structure of Typhoon Soudelor very clearly. After a series  
427 of pre-procedures such as the quality control, the bias correction, cloudy pixels are  
428 able to effectively be eliminated, ensuring the validity and rationality of the Ahi  
429 radiance data. The biases are also eliminated from the VarBC statistical method,  
430 which is able to provide a positive impact on the data assimilation procedure for the  
431 typhoon numerical simulation.

432 (2) Compared with the control experiment with only GTS data, the 3DVAR  
433 assimilation including AHI radiance data is able to improve the structure of typhoon's  
434 core and outer rain band. Also, the position and intensity of typhoon in the  
435 background field are able to be corrected.

436 (3) Generally, the track and minimum sea level pressure from the AHI radiance data  
437 assimilation experiment match better with the best track than the control experiment  
438 does for the subsequent 48-hour forecast. The maximum surface wind forecast error is

439 reduced only for the first 30-hour.

440 In this study, the AHI water radiance data assimilation is conducted under the  
441 clear sky condition. The results of the experiments indicate that AHI radiance data  
442 assimilation has a positive effect on the analysis and prediction of rapidly intensifying  
443 TC. Although, the whole developing stages of Typhoon Soudelor include a rapid  
444 intensification, a weakening, a second intensification, only the first intensification  
445 during 1 August to 4 August considered as the numerical period. It is worth  
446 investigating the impact of AHI data assimilation on the whole period including the  
447 first intensification, a weakening, and the second intensification of Typhoon Soudelor  
448 to fully prove the advantages of AHI radiance data assimilation. Considering the  
449 complex influence of underlying surface, only the rapid development stage of typhoon  
450 at sea were studied, while the whole generation, development and disappearance stage  
451 of typhoon can also be studied in the future. In addition, based on the AHI radiance  
452 data of the water vapor channels under the condition of clear sky, only 3DVAR  
453 method was adopted. Further improvements under the condition of all sky and hybrid  
454 DA can be obtained in the future.

#### 455 **Acknowledgments**

456 This research was primarily supported by the Chinese National Natural Science  
457 Foundation of China (G41805016), the Natural Science Foundation of Jiangsu  
458 Province (BK20170940), the Chinese National Natural Science Foundation of China  
459 (G41805070), the Chinese National Key R&D Program of China (2018YFC1506404,

460 2018YFC1506603), the research project of Heavy Rain and Drought-Flood Disasters  
461 in Plateau and Basin Key Laboratory of Sichuan Province in China (SZKT201901,  
462 SZKT201904), the research project of the Institute of Atmospheric Environment,  
463 China Meteorological Administration, Shenyang in China (2020SYIAE07,  
464 2020SYIAE02).

465

466

### References

467 Bauer, P., Geer, A.J., Lopez, P., and Salmond, D.: Direct 4D-Var assimilation of  
468 all-sky radiance. Part I: Implementation, Quarterly Journal of the Royal  
469 Meteorological Society, 136, 1868-1885, 2010.

470 Bauer, P., Auligné, T., Bell, W., Geer, A., Guidard, V., Heilliette, S., et al: Satellite  
471 cloud and precipitation assimilation at operational NWP centres, Quarterly Journal of  
472 the Royal Meteorological Society, 137, 1934-1951, 2011.

473 Bessho, K., Date, K., Hayashi, M., Ikeda, A., Imai, T., Inoue, H., et al.: An  
474 introduction to Himawari-8/9—Japan's new-generation geostationary meteorological  
475 satellites, Journal of the Meteorological Society of Japan, 94, 151-183, 2016.

476 Buehner, M., Caya, A., Carrieres, T., and Pogson, L.: Assimilation of SSMIS and  
477 ASCAT data and the replacement of highly uncertain estimates in the Environment  
478 Canada Regional Ice Prediction System, Quarterly Journal of the Royal  
479 Meteorological Society, 142, 562-573, 2016. Choi, Y., Cha, D.-H., Lee, M.-I., Kim,

480 J., Jin, C.-S., Park, S.-H., and Joh, M.-S.: Satellite radiance data assimilation for  
481 binary tropical cyclone cases over the western North Pacific, *J. Adv. Model. Earth*  
482 *Syst.*, 9, 832-853, 2017.

483 Dee, D.P., and Uppala, S.: Variational bias correction of satellite radiance data in the  
484 ERA–Interim reanalysis, *Quarterly Journal of the Royal Meteorological Society*, 135,  
485 1830-1841, 2009.

486 DeMaria, M., Sampson C.R., Knaff J.A., and Musgrave K.D.: Is tropical cyclone  
487 intensity guidance improving? *Bulletin of the American Meteorological Society*, 95,  
488 387-398, 2014.

489 Derber, J.C., and Wu, W.S.: The use of TOVS cloud–cleared radiance in the NCEP  
490 SSI analysis system, *Mon. Wea. Rev.*, 126, 2287-2299, 1998.

491 Di, D., Ai, Y., Li, J., Shi, W., and Lu, N.: Geostationary satellite-based 6.7  $\mu\text{m}$  band  
492 best water vapor information layer analysis over the Tibetan Plateau, *Journal of*  
493 *Geophysical Research: Atmospheres*, 121, 4600-4613, 2016.

494 Dudhia, J.: Numerical Study of Convection Observed during the Winter Monsoon  
495 Experiment Using a Mesoscale Two-Dimensional Model, *Journal of the Atmospheric*  
496 *Sciences*, 46, 3077-3107, 1989.

497 Geer, A. J., Baordo, F., Bormann, N., English, S., Kazumori, M., Lawrence, H., Lean,  
498 P., Lonitz, K., and Lupu, C.: The growing impact of satellite observations sensitive to  
499 humidity, cloud and precipitation, *Quart. J. Roy. Meteorol. Soc.*, 143, 3189-3206.

500 Goodman, S.J., Gurka, J., DeMaria, M., Schmit, T.J., Mostek, A., Jedlovec, G., et al.:



501 The GOES-R proving ground: Accelerating user readiness for the next-generation  
502 geostationary environmental satellite system, *Bulletin of the American Meteorological*  
503 *Society*, 93, 1029-1040, 2012.

504 Grell G.A., Dévényi D.: A generalized approach to parameterizing convection  
505 combining ensemble and data assimilation techniques, *Geophys. Res. Lett.*, 29,  
506 587-590, 2002.

507 Hilton, F., Atkinson, N. C., English, S. J., and Eyre, J. R.: Assimilation of IASI at the  
508 Met Office and assessment of its impact through observing system experiments,  
509 *Quarterly Journal of the Royal Meteorological Society*, 135, 495-505, 2009.

510 Hong S.Y., Noh Y., Dudhia J.: A New Vertical Diffusion Package with an Explicit  
511 Treatment of Entrainment Processes. *Mon. Wea. Rev.*, 134, 2318-2341, 2006.

512 Jung, J.A., Zapotocny, T.H., Le Marshall, J.F., and Treadon, R.E.: A two-season  
513 impact study on NOAA polar-orbiting satellites in the NCEP Global Data  
514 Assimilation System, *Weather Forecasting*, 23, 854-877, 2008.

515 Kamineni, R., Krishnamurti, T., Ferrare, R., Ismail, S., and Browell, E.: Impact of  
516 high resolution water vapor cross-sectional data on hurricane forecasting, *Geophysical*  
517 *Research Letters*, 30, 38-1, 2003. Kazumori, M.: Satellite radiance assimilation in the  
518 JMA operational mesoscale 4DVAR system, *Mon. Wea. Rev.*, 142, 1361-1381, 2014.

519 Li, X., and Zou, X.: Bias characterization of CrIS radiances at 399 selected channels  
520 with respect to NWP model simulations, *Atmospheric Research*, 196, 164-181, 2017.

521 Lim, K.-S. S., and Hong, S.-Y.: Development of an effective double-moment cloud  
522 microphysics scheme with prognostic cloud condensation nuclei (CCN) for weather  
523 and climate models. *Mon. Wea. Rev.*, 138, 1587-1612, 2010.

524 Liu, Z., Schwartz, C.S., Snyder, C., and Ha, S.Y.: Impact of assimilating AMSU-A  
525 radiance on forecasts of 2008 Atlantic tropical cyclones initialized with a limited-area  
526 ensemble Kalman filter, *Mon. Wea. Rev.*, 140, 4017-4034, 2012.

527 Liu, Q., and Weng, F.: Advanced doubling-adding method for radiative transfer in  
528 planetary atmosphere. *J. Atmos. Sci.*, 63, 3459–3465, 2006.

529 Ma, Z., Maddy E.S., Zhang B., Zhu T., and Boukabara S.A.: Impact Assessment of  
530 Himawari-8 AHI Data Assimilation in NCEP GDAS/GFS with GSI, *J. Atmos.*  
531 *Oceanic Technol.*, 34, 797-815, 2017.

532 McNally, A.P., Watts, P.D., Smith, J.A., Engelen, R., Kelly, G.A., Thépaut, J.N.,  
533 and Matricardi, M.: The assimilation of AIRS radiance data at ECMWF, *Quarterly*  
534 *Journal of the Royal Meteorological Society*, 132, 935-957, 2006.

535 Minamide, M., and Zhang F.: Assimilation of all-sky infrared radiances from  
536 himawari-8 and impacts of moisture and hydrometer initialization on  
537 convection-permitting tropical cyclone prediction. *Mon. Wea. Rev.*, 146, 3241-3258,  
538 2018.

539 Mlawer E.J., Taubman S.J., Brown P.D., et al.: Radiative transfer for inhomogeneous  
540 atmospheres: RRTM, a validated correlated-k model for the longwave, *Journal of*

541 Geophysical Research Atmospheres, 102, 16663-16682, 1997.

542 Montmerle, T., Rabier, F., and Fischer, C.: Relative impact of polar-orbiting and  
543 geostationary satellite radiance in the Aladin/France numerical weather prediction  
544 system, Quarterly Journal of the Royal Meteorological Society, 133, 655-671, 2007.

545 Noh Y., Cheon W.G., Hong S.Y., et al.: Improvement of the K-profile Model for the  
546 Planetary Boundary Layer based on Large Eddy Simulation Data, Boundary-Layer  
547 Meteorology, 107, 401-427, 2003.

548 Prunet, P., Thépaut, J.N., Cassé, V., Pailleux, J., Baverez, A., and Cardinali,  
549 C.: Strategies for the assimilation of new satellite measurements at Météo-  
550 France, Advances in Space Research, 25, 1073-1076, 2000.

551 Qin, Z., Zou, X., Weng, F.: Evaluating Added Benefits of Assimilating GOES Imager  
552 Radiance Data in GSI for Coastal QPFs, Mon. Wea. Rev, 141, 75-92, 2013.

553 Rennie, M.P.: The impact of GPS radio occultation assimilation at the Met  
554 Office, Quarterly Journal of the Royal Meteorological Society, 136, 116-131, 2010.

555 Schmit, T.J., Gunshor, M.M., Paul Menzel, W., Gurka, J., Li, J., and Bachmeier,  
556 S.: Introducing the next-generation advanced baseline imager (ABI) on  
557 GOES-R, Bulletin of the American Meteorological Society, 86, 1079-1096, 2005.

558 Schmit, T.J., Li, J., Li, J., Feltz, W.F., Gurka, J.J., Goldberg, M.D., and Schrab,  
559 K.J.: The GOES-R Advanced Baseline Imager and the continuation of current sounder  
560 products, Journal of Applied Meteorology and Climatology, 47, 2696-2711, 2008.

561 Schmit, T.J., Griffith, P., Gunshor, M.M., Daniels, J.M., Goodman, S.J., and Lehair,  
562 W.J.: A closer look at the ABI on the GOES-R series, *Bulletin of the American*  
563 *Meteorological Society*, 98, 681-698, 2017.

564 Schwartz, C. S., Liu, Z., Chen, Y. and Huang X.-Y.: Impact of assimilating  
565 microwave radiances with a limited - area ensemble data assimilation system on  
566 forecasts of Typhoon Morakot, *Weather Forecasting*, 27, 424-437, 2012.

567 Shen, F., and Min, J.: Assimilating AMSU-A radiance data with the WRF hybrid  
568 En3DVAR system for track predictions of Typhoon Megi (2010), *Advances in*  
569 *Atmospheric Sciences*, 32, 1231-1243, 2015.

570 Song J-J, Wang Y, Wu L.: Trend discrepancies among three best track data sets of  
571 western North Pacific tropical cyclones. *J. Geophys. Res.* 115: D12128, DOI:  
572 10.1029/2009JD013058, 2010.

573 Stengel, M., Undén, P., Lindskog, M., Dahlgren, P., Gustafsson, N., and Bennartz, R.:  
574 Assimilation of SEVIRI infrared radiance with HIRLAM 4D-Var, *Quarterly Journal*  
575 *of the Royal Meteorological Society*, 135, 2100-2109, 2009.

576 Wang, Y., Liu, Z., Yang, S., Min, J., Chen, L., Chen, Y., and Zhang, T.: Added value of  
577 assimilating Himawari-8 AHI water vapor radiances on analyses and forecasts for  
578 “7.19” severe storm over north China, *Journal of Geophysical Research: Atmospheres*,  
579 123, 3374-3394, 2018.

580 Xu, D., Liu, Z., Huang, X.-Y., Min, J., and Wang, H.: Impact of assimilation IASI

581 radiances on forecasts of two tropical cyclones, *Meteorology and Atmospheric*  
582 *Physics*, 122, 1-18, 2013.

583 Xu, D., Huang, X.-Y., Wang H., Mizzi, A. P. and Min J.: Impact of assimilating  
584 radiances with the WRFDA ETKF/3DVAR hybrid system on prediction of two  
585 typhoons in 2012, *J. Meteorol. Res*, 29, 28-40, 2015.

586 Yan, B., Weng, F., and Derber, J. Assimilation of satellite microwave water vapor  
587 sounding channel data in NCEP Global Forecast System (GFS), paper presented at  
588 17th International TOVS Study Conference, Int. ATOVS Working Group, Monterrey,  
589 Calif, 2010.

590 Yang, C., Liu, Z., Bresch, J., Rizvi, S. R. H, Huang, X.-Y., and Min, J.: AMSR2  
591 all-sky radiance assimilation and its impact on the analysis and forecast of Hurricane  
592 Sandy with a limited-area data assimilation system, *Tellus A: Dynamic Meteorology*  
593 *and Oceanography*, 68, 2016.

594 Yu H, Hu C, Jiang L.: Comparison of three tropical cyclone intensity datasets. *Acta*  
595 *Meteorol. Sin.* 21, 121-128, 2007.

596 Zapotocny, T.H., Jung, J.A., Le Marshall, J.F., and Treadon, R.E.: A two-season  
597 impact study of satellite and in situ data in the NCEP Global Data Assimilation  
598 System, *Weather Forecasting*, 22, 887-909, 2007.

599 Zhu, Y., Derber, J., Collard, A., Dee, D., Treadon, R., Gayno, G., and Jung,  
600 J.A.: Enhanced radiance bias correction in the National Centers for Environmental  
601 Prediction's Gridpoint Statistical Interpolation data assimilation system, *Quarterly*

602 Journal of the Royal Meteorological Societ, 140, 1479-1492, 2014.

603 Zou, X., Qin, Z., and Weng, F.: Improved coastal precipitation forecasts with direct

604 assimilation of GOES-11/12 imager radiance, Mon. Wea. Rev, 139, 3711-3729, 2011.

605 Zou, X., Qin Z., and Zheng Y.: Improved tropical storm forecasts

606 with GOES-13/15 imager radiance assimilation and asymmetric vortex initialization

607 in HWRF, Mon. Wea. Rev, 143, 2485-2505, 2015.

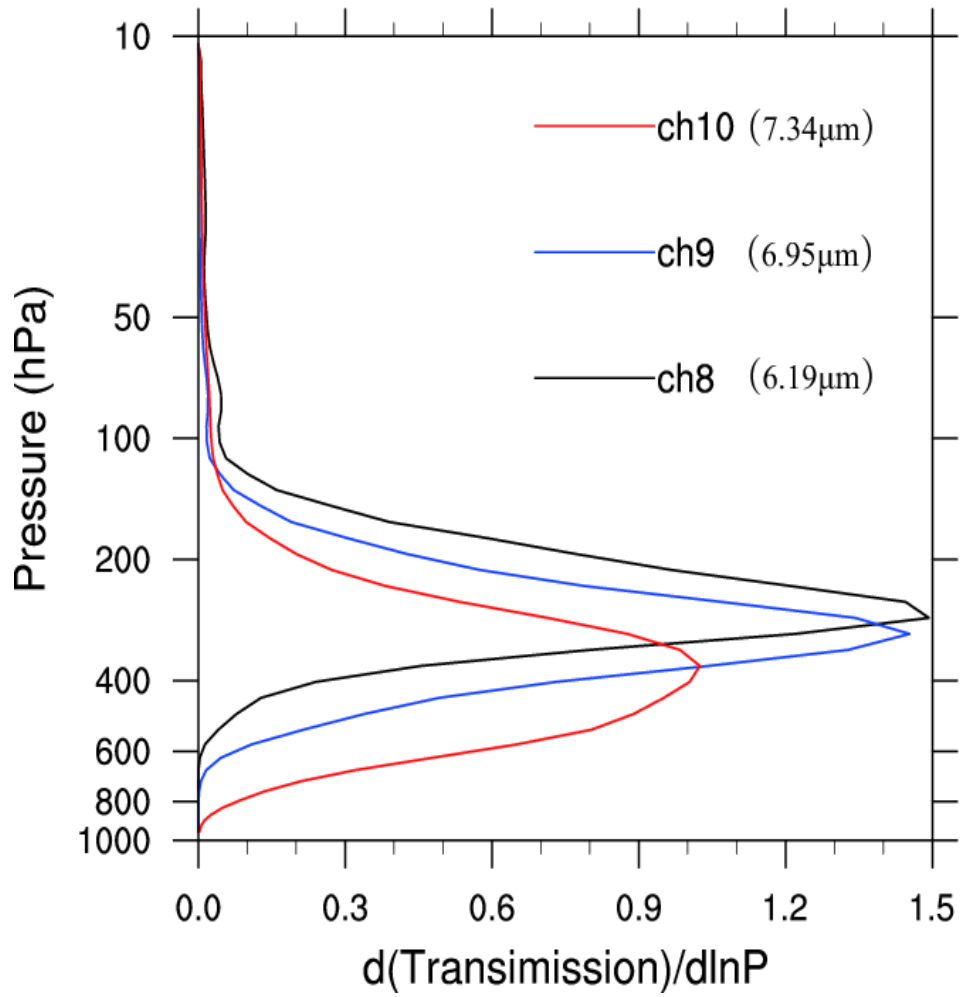
608

609

610

### **List of Figures**

611



612

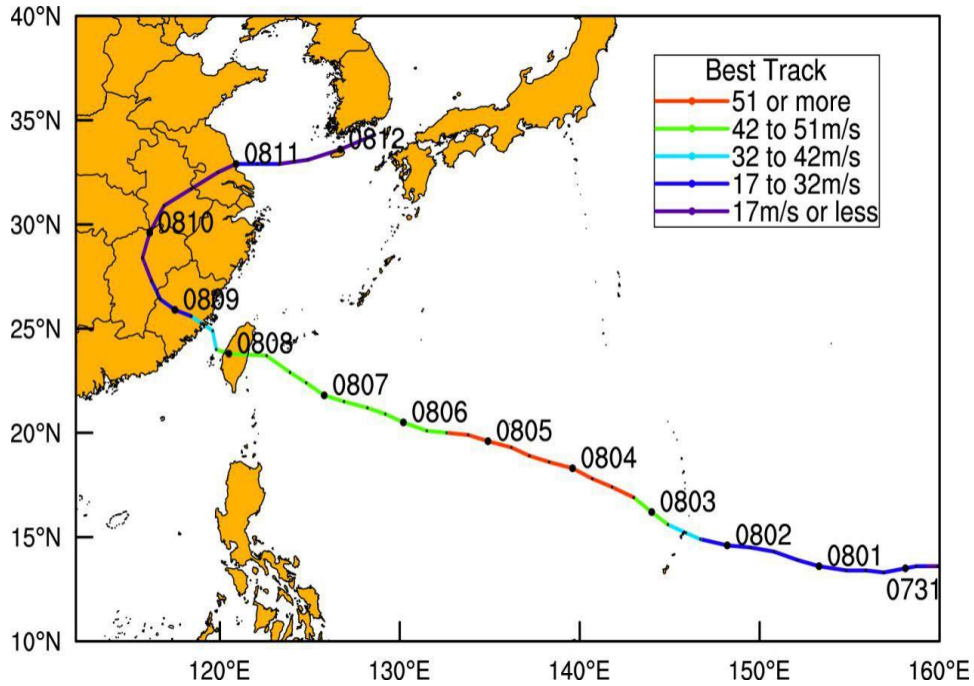
613 Fig.1 Weighting functions of Himawari-8 Advanced Himawari Imager three water  
 614 vapor channels for Channel 8, 9, and 10.

615

616

617

618



619

620 Fig.2 The best track of Soudelor from the China Meteorological Administration  
 621 (CMA) from 0000 UTC 30 July to 0600 UTC 12 August 2015. Different colors  
 622 represent intensity changes.

623

624

625

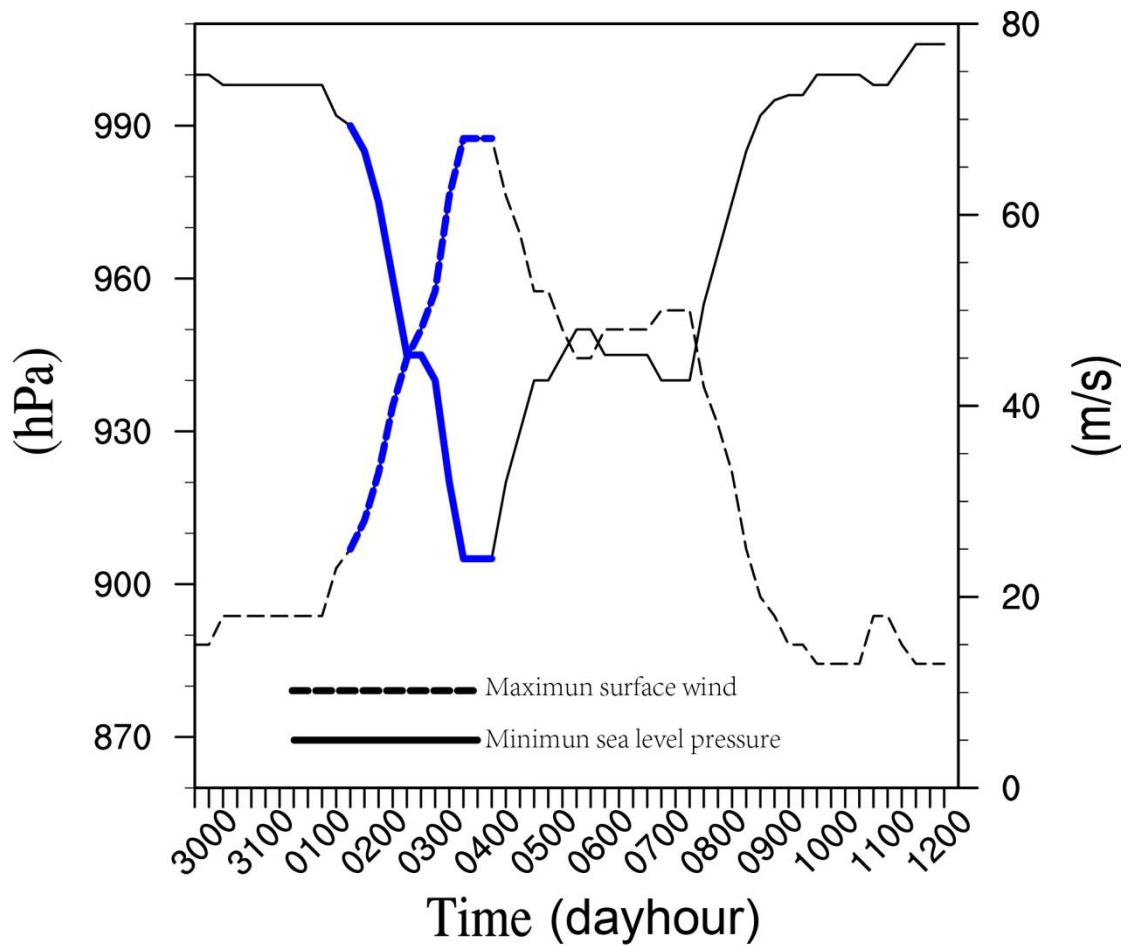
626

627

628

629





630

631 Fig. 3 The time series of the minimum sea level pressure (solid line, unit: hPa) and the  
 632 maximum surface wind (dash line, unit:  $\text{m s}^{-1}$ ) of Typhoon Soudelor from the CMA  
 633 best-track data from 0000 UTC 30 July 2015 to 0600 UTC 12 August 2015. The  
 634 specific period for the numerical results from 1800 UTC 1 August 2015 to 0600 UTC  
 635 4 August 2015 is highlighted in blue.

636

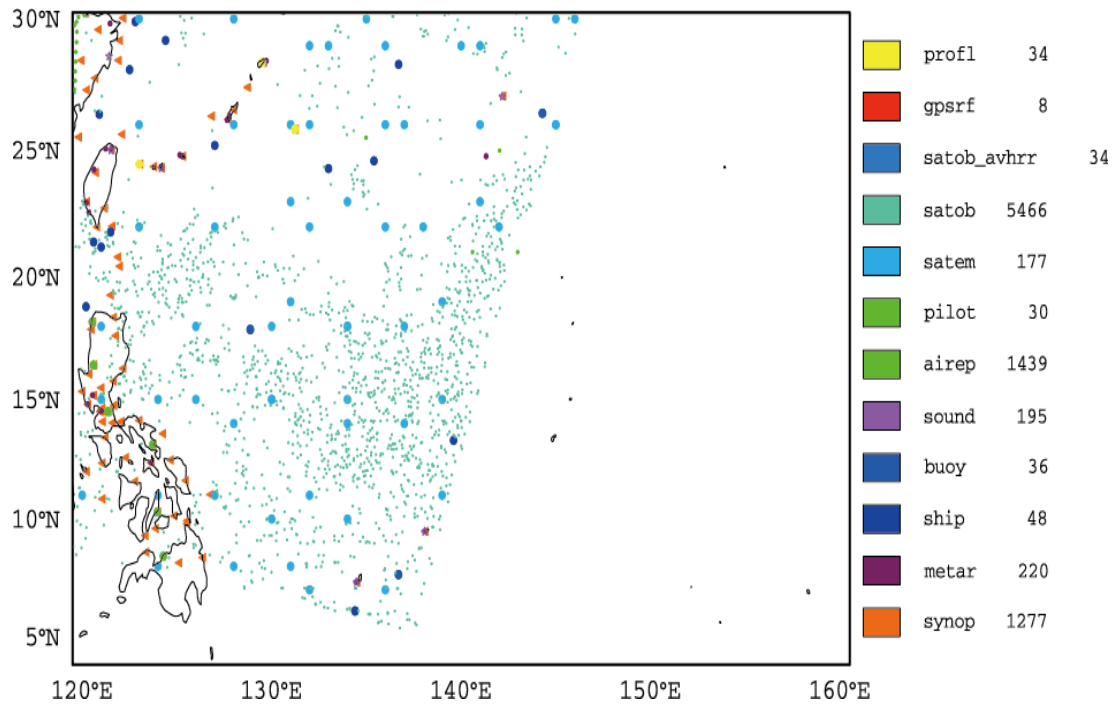
637

638

639

640

641



642

643 Fig. 4 Distribution of GTS observations in the simulated area at 0000 UTC 2 August

644 2015. On the right side of the map is the name of observation data and the number of

645 observations. Each observation type is marked with different color along with a

646 unique symbol.

647

648

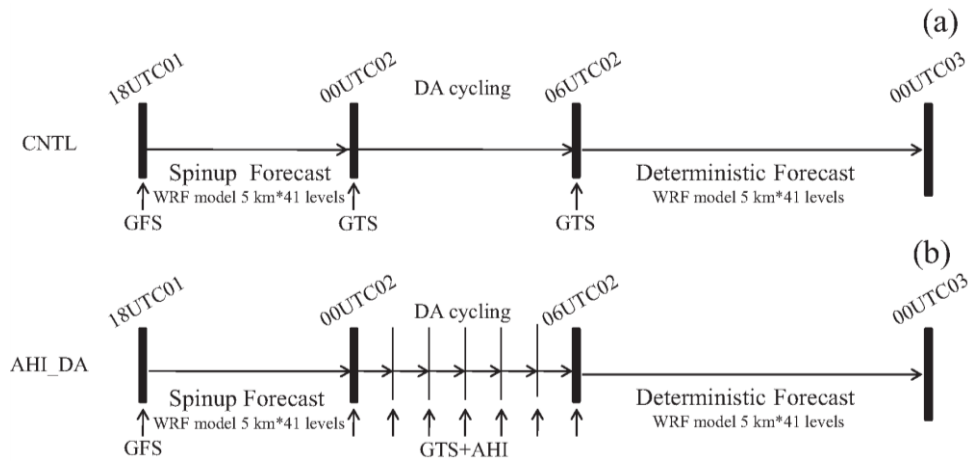
649

650

651

652

653



654

655 Fig. 5 The flow chart of the data assimilation experiments. (a) CNTL, (b) AHI\_DA

656

657

658

659

660

661

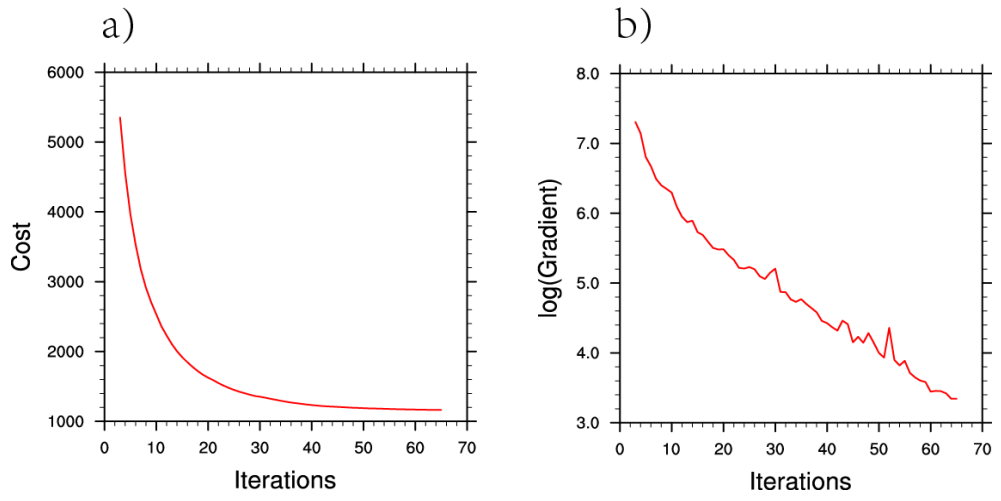
662

663

664

665

666



667

668 Fig. 6 (a) Cost function as functions of iterations, (b) gradient as functions of  
669 iterations.

670

671

672

673

674

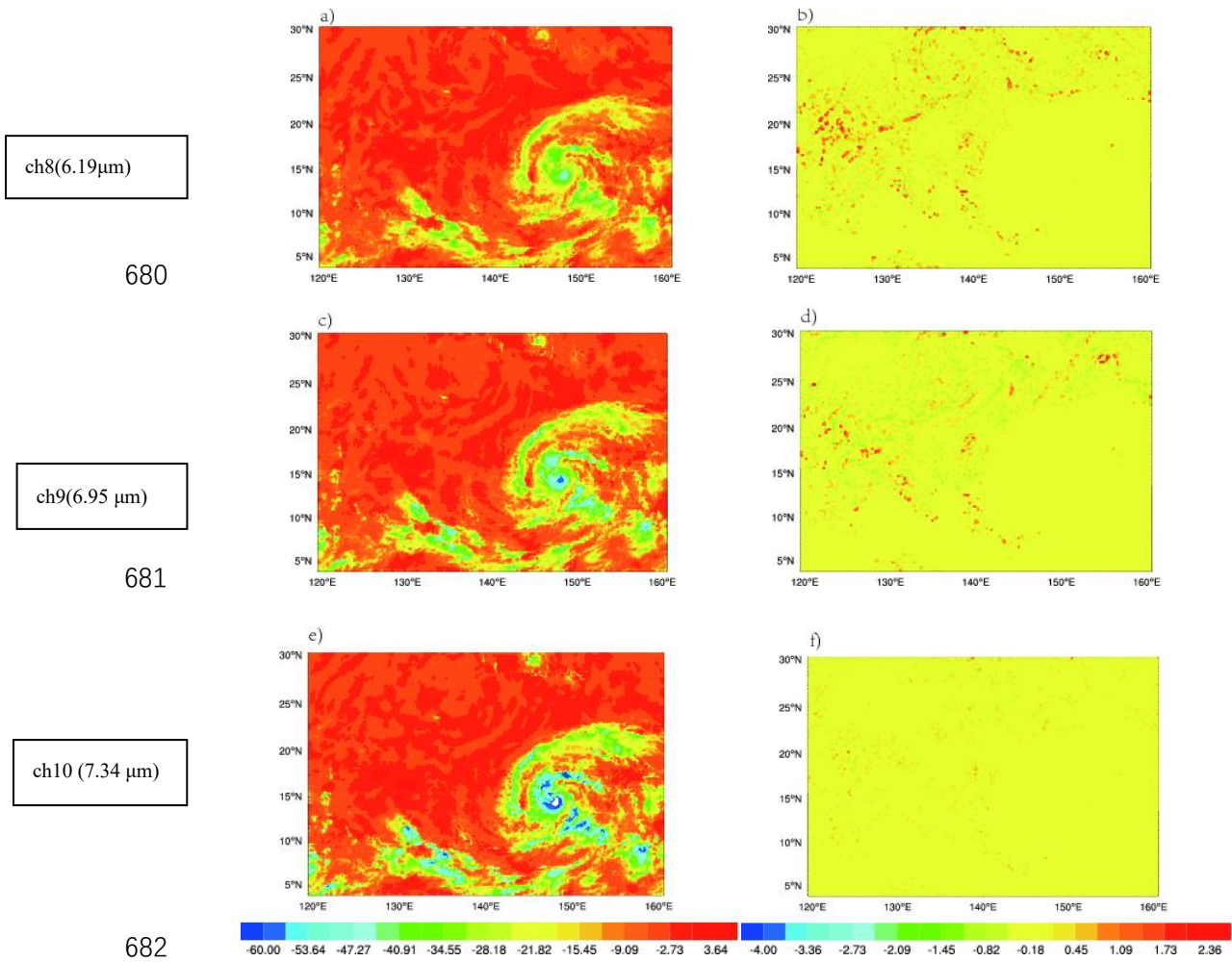
675

676

677

678

679



683 Fig. 7 (a, c, and e) OMB (unit: K) after bias correction for channel 8, 9, and 10,  
684 respectively; (b, d, and f) OMA (unit: K) after bias correction for channel 8, 9, and 10,  
685 respectively at 0000 UTC 2 August 2015.

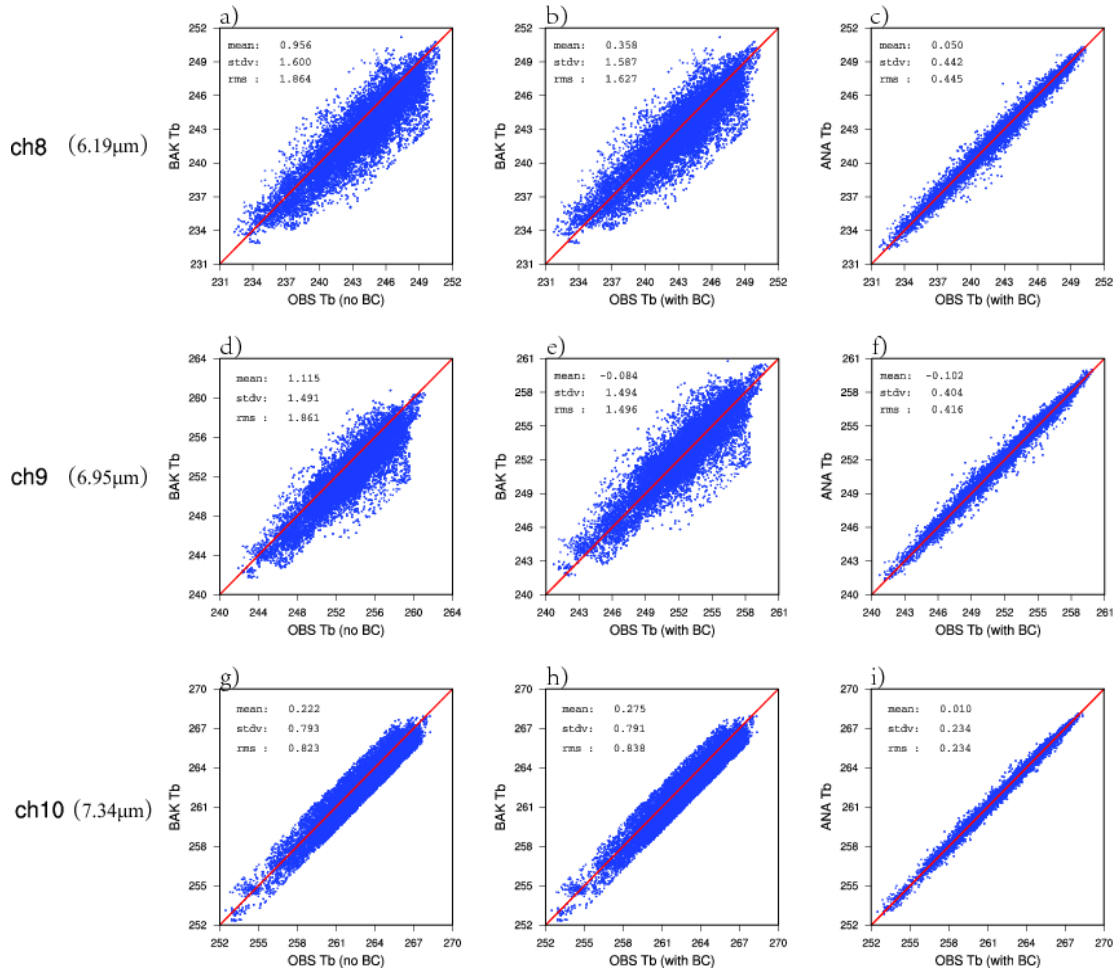
686

687

688

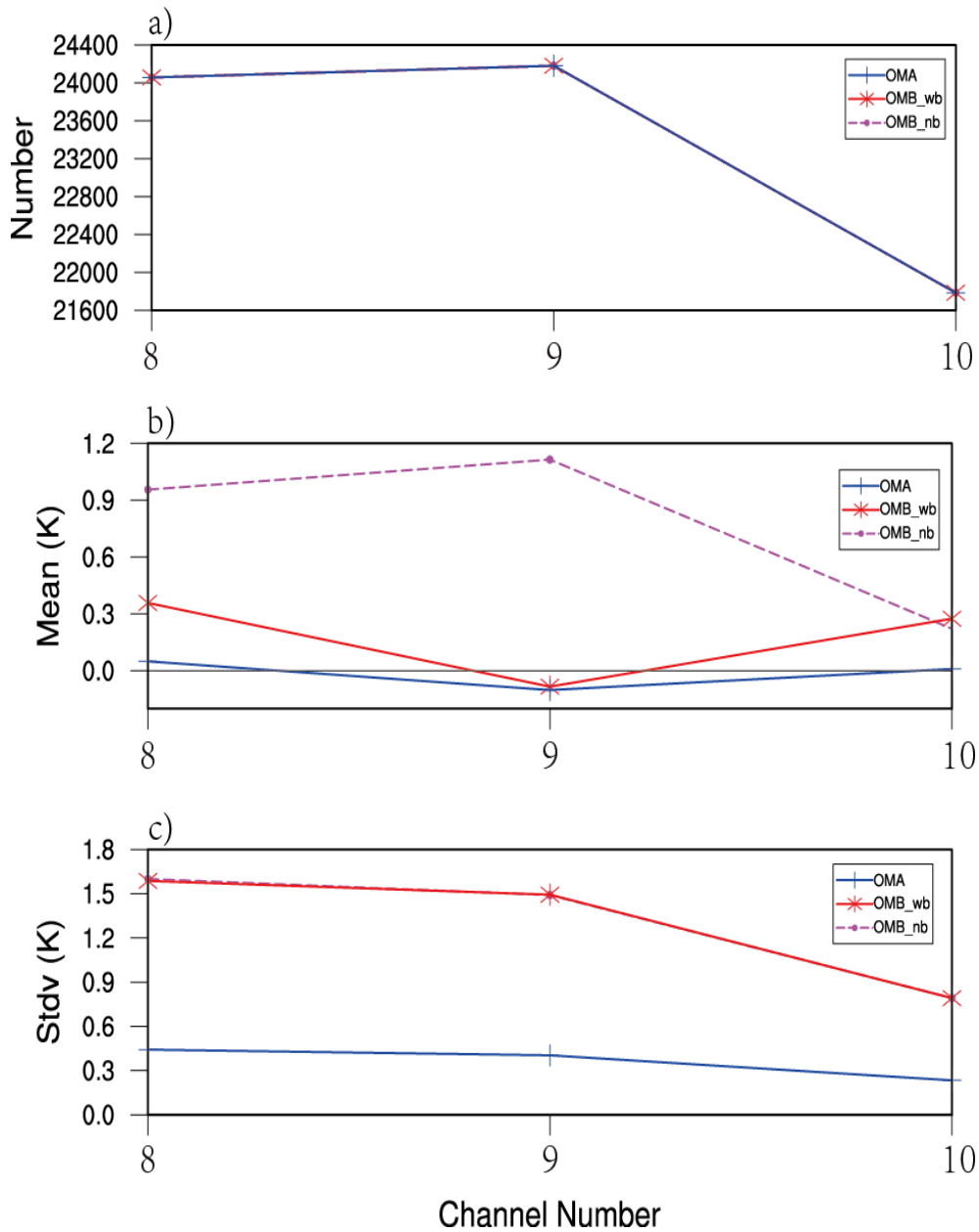
689

690



691

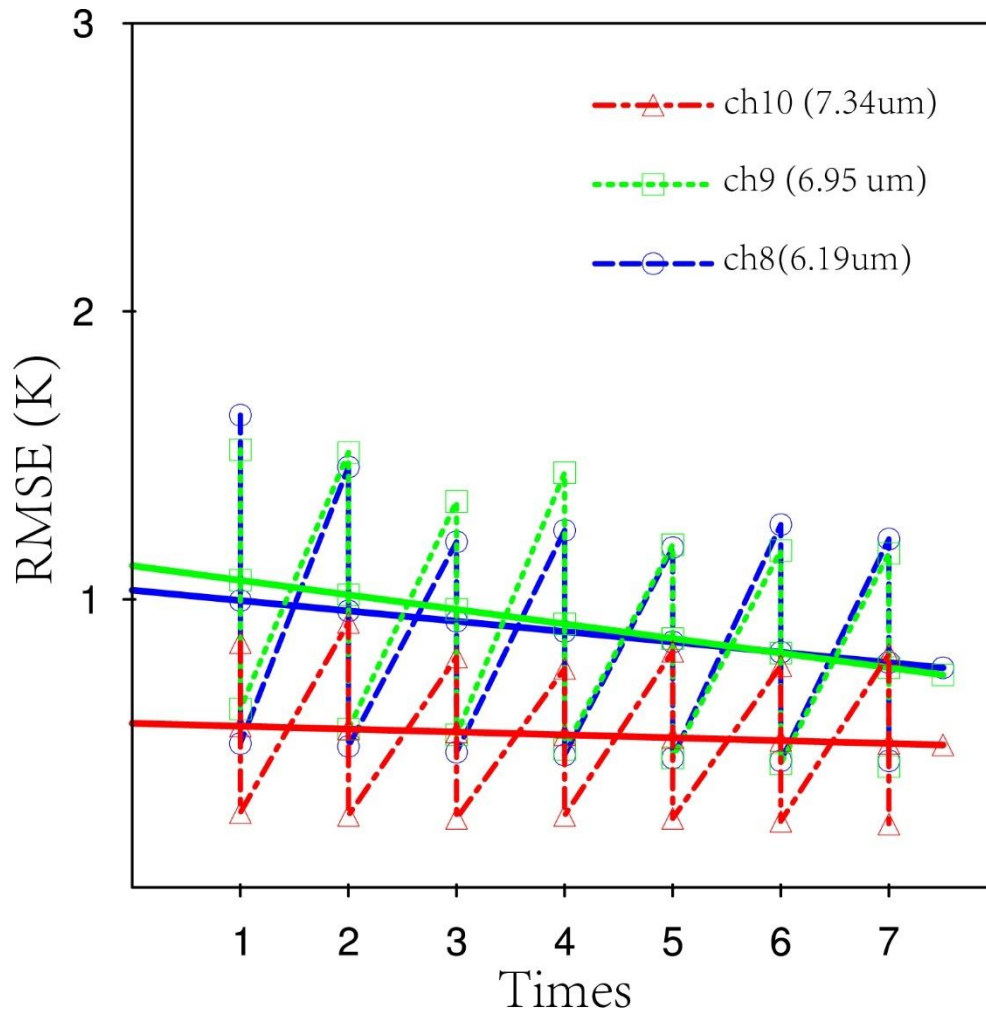
692 Fig. 8 Scatter plots of (a, d and g) the observed and background brightness  
693 temperature before the bias correction of channel 8, 9 and 10. Scatter plots of (b, e  
694 and h) the observed and background brightness temperature after the bias correction  
695 of channel 8, 9 and 10. Scatter plots of (c, f and i) the observed and analyzed  
696 brightness temperature after the bias correction of channel 8, 9 and 10.



697

698 Fig. 9 Number of (a) observations, (b) mean (unit: K), and (c) standard deviations  
 699 (unit: K) of OMB and OMA before and after the bias correction for water vapor  
 700 channels 8-10 (OMB\_nb: OMB without bias correction; OMB\_wb: OMB with bias  
 701 correction).

702



703

704 Fig.10 Time series of the RMSE for the brightness temperature (unit: K) with  
 705 assimilation times before and after the data assimilation along with the trend lines.

706

707

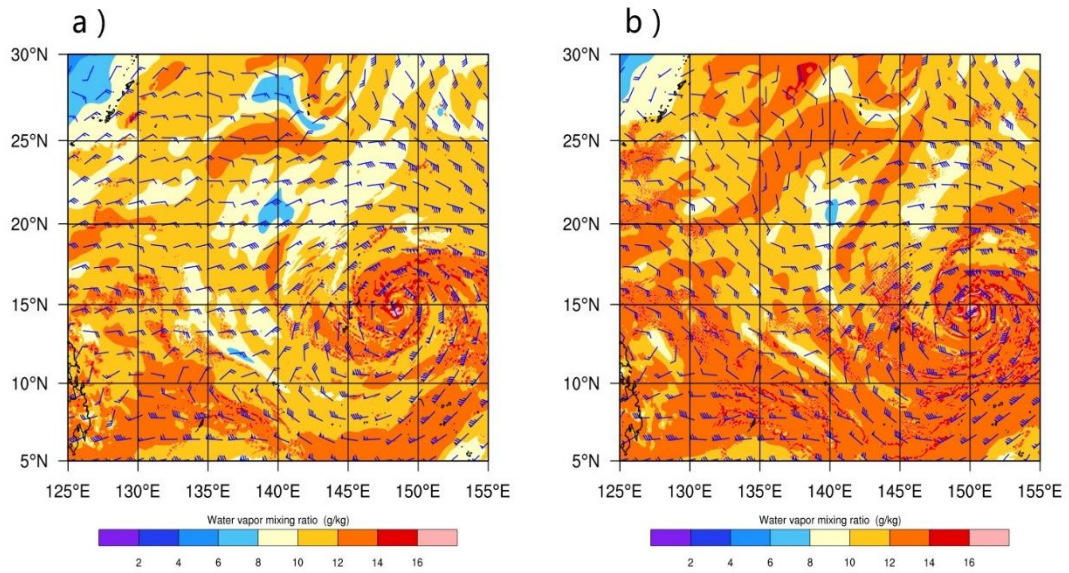
708

709

710



711



712

713 Fig. 11 The surface wind speed (vectors, unit:  $\text{m s}^{-1}$ ) and water vapor (colored, unit:  
714  $\text{g/kg}$ ) for (a) CTNL; (b) AHI\_DA at 850 hPa at 0000 UTC 2 August 2015.

715

716

717

718

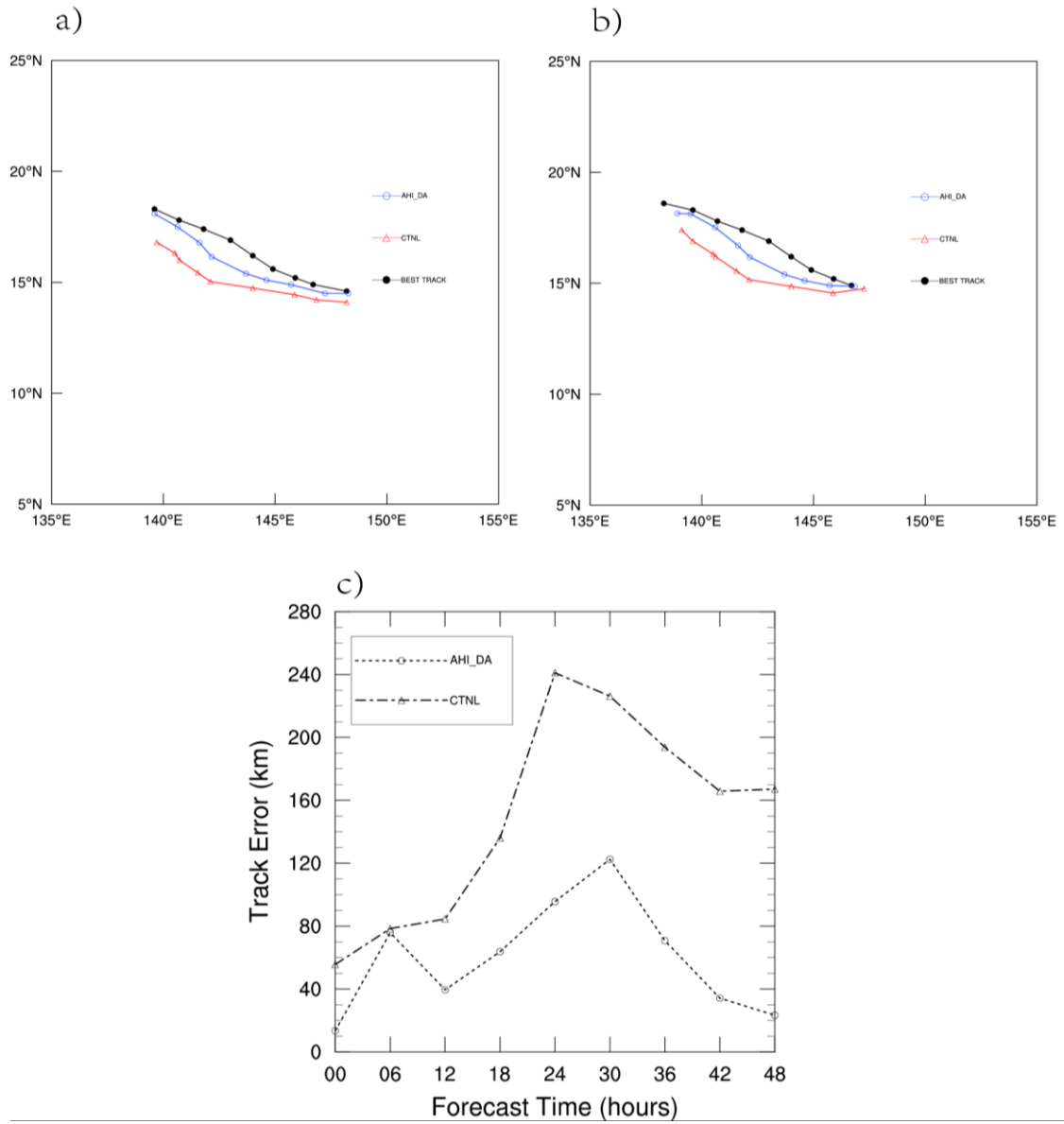
719

720

721

722

723



724

725

726 Fig. 12 The 48-hour predicted tracks (a) from 0000 UTC 2 August to 0000 UTC 4

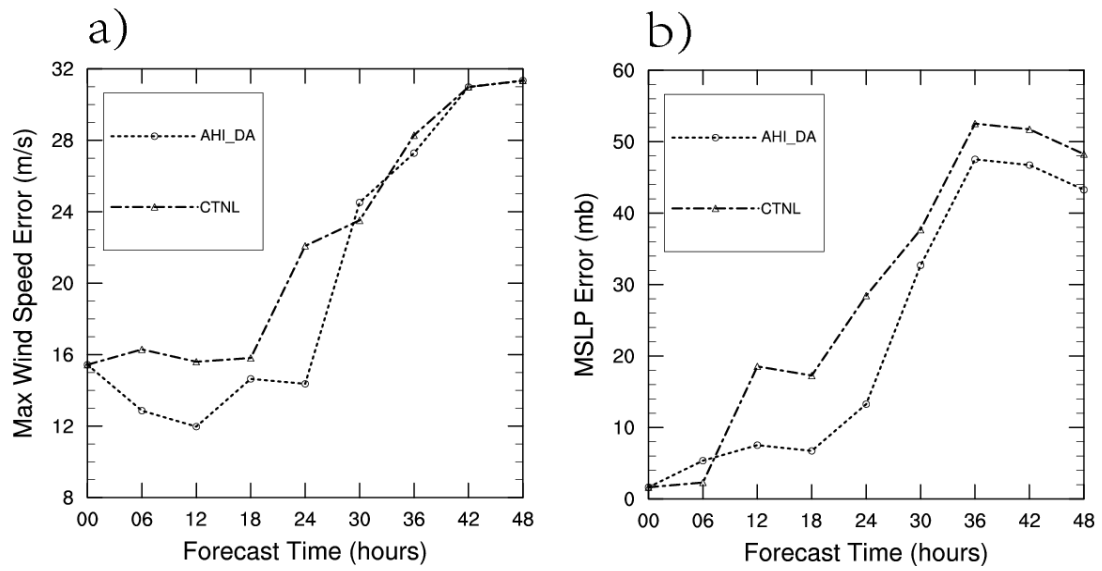
727 August, (b) from 0600 UTC 2 August to 0600 UTC 4 August 2015, (c) averaged track

728 errors (unit: km) for the two forecasts.

729

730

731



732

733 Fig.13 The 48-hour (a) maximum surface wind error (unit:  $\text{m s}^{-1}$ ), (b) minimum sea  
734 level pressure error (unit: hPa) of Soudelor (2015) averaged from two forecasts.

735